J. Fluid Mech. (1993), *vol.* 256, *pp.* 1–25

A numerical investigation of the coherent vortices in turbulence behind a backward-facing step

By ARISTEU SILVEIRA NETO[1,2,3], DOMINIQUE GRAND[2], OLIVIER MÉTAIS[3] AND MARCEL LESIEUR[3]

[1] Departamento de Engenharia Mecânica, UFU, Uberlândia, M.G. 38400, Brazil

[2] Commissariat à l'Energie Atomique, D.R.N., Centre d'Etudes Nucléaires de Grenoble, Service des Transferts Thermiques/LPML, BP 85 X, 38041 Grenoble Cedex, France

[3] Institut de Mécanique de Grenoble/LEGI (URA CNRS 1509), Institut National Polytechnique de Grenoble *and* Université Joseph Fourier, Grenoble, BP 53 X, 38041 Grenoble Cedex, France

(Received 3 July 1991 and in revised form 8 April 1993)

This paper presents a statistical and topological study of a complex turbulent flow over a backward-facing step by means of direct and large-eddy simulations. Direct simulations are first performed for an isothermal two-dimensional case. In this case, shedding of coherent vortices in the mixing layer is demonstrated. Both direct and large-eddy simulations are then carried out in three dimensions. The subgrid-scale model used is the structure-function model proposed by Métais & Lesieur (1992). Low-step computations corresponding to the geometry of Eaton & Johnston's (1980) laboratory experiment give turbulence statistics in better agreement with the experimental data than both Smagorinsky's method and $K-\epsilon$ modelling. Furthermore, calculations for a high step show that the eddy structure of the flow presents striking analogies with forced plane mixing layers: large billows are shed behind the step with intense longitudinal vortices strained between them.

1. Introduction

For many years, turbulence in fluids has been the object of uninterrupted efforts aimed at unveiling the mystery of its dynamics. An important idea which has recently emerged is the concept of coherent vortices, corresponding to local vorticity concentration of lifetime much longer than its turnover time. This concept is linked to important improvements in visualization techniques, both in laboratory and numerical experiments.

These coherent structures play an important role in numerous technological applications: thermohydraulics in nuclear reactors, environmental studies, acoustics, vibrations, aerodynamics, combustion, etc. In each of these fields, it is necessary to understand the dynamics of these organized motions so as to mechanically control their production or suppression.

In high-Reynolds-number mixing layers, Kelvin–Helmholtz coherent vortices were identified by Brown & Roshko (1974). More recent laboratory experiments (Breidenthal 1981; Bernal & Roshko 1986; Lasheras & Choi 1988), have indicated that mixing layers exhibit a three-dimensional character, for instance in the form of thin hairpin vortex filaments which are strained between the quasi-two-dimensional large vortices. The same vortices have been found in the computations carried out by Metcalfe *et al.* (1987).

Although the numerical simulation of coherent structures has greatly improved, it is

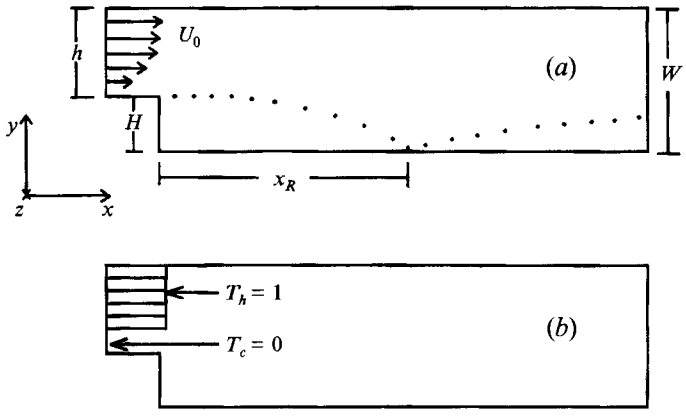

FIGURE 1. Computational domain, geometric characteristics and inlet boundary conditions: (*a*) velocity profile; (*b*) temperature profile.

still compulsory, at high Reynolds number, to model the subgrid scales: this is the large-eddy simulation approach proposed by Smagorinsky (1963), Lilly (1967) and Deardorff (1970). The large-eddy simulation approach has been used in various domains of turbulence such as three-dimensional isotropic turbulence decay (Lesieur & Rogallo 1989), the turbulent channel (Moin & Kim 1982), and the compressible boundary layer at high Mach number (Normand & Lesieur, 1992). The results obtained were encouraging enough to justify the present study dealing with the incompressible flow over a backward-facing step in a plane channel (see figure 1*a*). Although the geometry remains simple, some features of complex turbulent shear flows such as separation, curvature, re-circulation and re-attachment are present.

Other numerical studies dealing with separated flows in various geometries have been performed (see e.g. Arnal & Friedrich 1993, for the backward-facing step; Werner & Wengle 1993, for the flow over and around a cube). In the present paper, particular attention is given to the detailed investigation of the flow structures, while also considering flow statistics. The paper is organized as follows: governing equations and numerical methods are presented in §2. This section presents in particular the various boundary conditions and flow geometries that have been considered in the numerical experiments. The analysis of the organized vortex structures encountered in both two- and three-dimensional simulations is performed in §3. Section 4 focuses on the statistical properties of the turbulent field. In this section, we consider a flow geometry close to Eaton & Johnston's (1980) laboratory experiment, and compare the numerical results to the available experimental ones.

2. Numerical methods and flow configuration

2.1. *Governing equations*

In a large-eddy simulation, each variable f is decomposed into two parts: one related to the large-scale field, $\bar{f}$, and the other related to the subgrid-scale field, f', i.e.

$$f = \bar{f} + f'. \tag{2.1}$$

Following Leomard (1974), the large-scale field is defined with the aid of the filter G:

$$\bar{f}(\boldsymbol{x}) = \int_D G(\boldsymbol{x}-\boldsymbol{x}')f(\boldsymbol{x}')\,\mathrm{d}\boldsymbol{x}', \tag{2.2}$$

where D is the integration control domain. In our study, G is the classical *box filter* used by Deardorff (1970) and by Clark, Ferziger & Reynolds (1979):

$$G(x-x') = \begin{cases} (1/\Delta)^3, & |x_i - x_i'| \leqslant (\frac{1}{2}\Delta) \\ 0, & |x_i - x_i'| > (\frac{1}{2}\Delta), \end{cases} \tag{2.3}$$

where $i = 1, 2, 3$ and Δ is the characteristic filter length. For the finite-volume discretization method used in this study,

$$\Delta = \left[\prod_{i=1}^{3} \Delta x_i\right]^{\frac{1}{3}},$$

where Δx_i is the computational mesh size in the i-direction; the indices $i = 1, 2, 3$ refer respectively to the streamwise, normal and spanwise direction. The filtering and partial-differentiation operators obey the commutative property:

$$\frac{\overline{\partial f}}{\partial x_i} = \frac{\partial \overline{f}}{\partial x_i}. \tag{2.4}$$

Now, we apply the filter G to the incompressible Navier–Stokes equation, which gives

$$\frac{\partial \overline{u}_i}{\partial t} + \frac{\partial}{\partial x_j}(\overline{u}_i \overline{u}_j) = -\frac{1}{\rho_0}\frac{\partial \overline{p}}{\partial x_i} + \frac{\partial}{\partial x_j}[2\nu S_{ij} + \tau_{ij} - L_{ij} - C_{ij}], \tag{2.5}$$

$$\frac{\partial \overline{u}_i}{\partial x_i} = 0, \tag{2.6}$$

where L_{ij} are the Leonard stresses, C_{ij} the cross-stresses, τ_{ij} the subgrid Reynolds stresses and S_{ij} the strain rate of the filtered velocity field:

$$\left.\begin{aligned} L_{ij} &= \overline{\overline{u}_i \overline{u}_j} - \overline{u}_i \overline{u}_j, \quad C_{ij} = \overline{\overline{u}_i u_j'} + \overline{u_i' \overline{u}_j}, \\ \tau_{ij} &= -\overline{u_i' u_j'}, \quad S_{ij} = \tfrac{1}{2}(\partial \overline{u}_i/\partial x_j + \partial \overline{u}_j/\partial x_i). \end{aligned}\right\} \tag{2.7}$$

While τ_{ij} and C_{ij} must be modelled, L_{ij} can either be modelled or directly computed, as will be seen later. The subgrid Reynolds stresses τ_{ij} are evaluated through the structure function model (Métais & Lesieur 1992) presented below. We will show later that C_{ij} and L_{ij} may be neglected.

2.2. *Structure-function subgrid model*

One can write

$$\tau_{ij} = -\overline{u_i' u_j'} = 2\nu_t S_{ij} - \tfrac{2}{3} K_s \delta_{ij}, \tag{2.8}$$

where K_s is the subgrid kinetic energy. In the spectral eddy viscosity approach for isotropic turbulence, a cutoff wavenumber in Fourier space $k_c = \pi/\Delta$ is defined. Let $E(k_c)$ be the kinetic energy spectrum. An 'à la mixing length' argument gives

$$\nu_t \sim k_c^{-1} v(k_c) \sim k_c^{-1}[k_c E(k_c)]^{\frac{1}{2}} = C[E(k_c)/k_c]^{\frac{1}{2}}, \tag{2.9}$$

where $v(k_c)$ is the characteristic turbulent velocity in the subgrid scales. C is a constant to be determined. Non-local expansions based upon the EDQNM theory, plus the assumption of a $k^{-\frac{5}{3}}$ spectrum for $k > k_c$, yield for $k \ll k_c$ (Lesieur 1990): $C = 0.44 C_K^{-\frac{3}{2}}$, where C_K is the Kolmogorov constant. In fact, this eddy-viscosity evaluation is no longer valid close to k_c due to the existence of a cusp (Kraichnan 1976). A simpler approach consists in the 'averaged spectral eddy viscosity' (without cusp), where C is evaluated using kinetic-energy conservation arguments, which yields $C = \frac{2}{3} C_K^{-\frac{3}{2}}$.

In the structure-function model, one works in physical space: the averaged spectral eddy viscosity is evaluated with the aid of a local kinetic-energy spectrum $E_x(k_c)$. The latter is calculated in terms of the local second-order velocity structure function

$$F_2(x, \Delta, t) = \langle \|u(x,t) - u(x+r,t)\|^2 \rangle_{\|r\|=\Delta} \tag{2.10}$$

using the 'Batchelor–Orszag formula'

$$F_2(x, \Delta, t) = 4.82 C_K (\epsilon \Delta)^{\frac{2}{3}}, \quad E_x(k_c) = C_K \epsilon^{\frac{2}{3}} (\pi/\Delta)^{-\frac{5}{3}}, \tag{2.11}$$

which yields

$$E_x(k_c) = \frac{1}{4.82} \pi^{-\frac{5}{3}} \Delta F_2(x, \Delta, t). \tag{2.12}$$

Expressing the structure function of the filtered field, $\bar{F}_2$, in terms, of the structure function of the instantaneous field, one finally obtains (see Métais & Lesieur 1992 for details)

$$\nu_t(x, \Delta, t) = 0.104 C_K^{-\frac{3}{2}} \Delta [\tilde{F}_2(x, \Delta, t)]^{\frac{1}{2}}. \tag{2.13}$$

It is this expression that will be used as a subgrid-scale model in the remainder of the present study.

For isotropic turbulence where spatial intermittency exists, this model gives kinetic energy spectra in better agreement with Kolmogorov's law than models such as Smagorinsky's. It can also be used for inhomogeneous flows, where the small scales are not too far from isotropy, while the large-scale inhomogeneities are directly taken into account by the simulation. In practical cases, and for a regular cubic mesh, the local structure function is obtained from an arithmetic average of the contributions coming from the six closest surrounding points, distributed in the three spatial directions.

The subgrid kinetic energy K_s appearing in (2.8) is defined by

$$K_s \equiv \int_{k_c=\pi/\Delta}^{\infty} E(k,t)\, \mathrm{d}k, \tag{2.14}$$

which turns out to be

$$K_s(x, \Delta, t) = 0.37 \bar{F}_2(x, \Delta, t). \tag{2.15}$$

The problem can also be envisaged by incorporating the subgrid kinetic energy into the pressure term, as in Métais & Lesieur (1992). We have performed calculations with both methods, without any difference in the results.

As previously noted, the Leonard stresses L_{ij} and the cross-stresses C_{ij} can also be modelled. Clark *et al.* (1979) determine these quantities through a Taylor series expansion of $\overline{\bar{u}_i \bar{u}_j}$ about the centre of the control volume surrounding x. Following this idea, Findikakis & Street (1979) demonstrate that $L_{ij} + C_{ij}$ can be approximated by

$$L_{ij} + C_{ij} \approx \frac{\Delta_l}{12} \frac{\partial \bar{u}_i}{\partial x_l} \frac{\partial \bar{u}_j}{\partial x_l}, \tag{2.16}$$

where $l = 1, 2, 3$.

We will use this expression to calculate $L_{ij} + C_{ij}$ and compare it with the subgrid Reynolds stresses, the velocity derivatives being taken from the present large-eddy simulation. Therefore, the following quantities are defined

$$D_R = \overline{\|\nabla \cdot \tau_{ij}\|}, \quad D_L = \overline{\|\nabla \cdot (L_{ij} + C_{ij})\|}, \quad D_M = \overline{\|\nabla \cdot (2\nu S_{ij})\|}, \tag{2.17}$$

the overbar denoting a temporal mean. The results are shown on figure 2, where the maxima of D_R, D_L and D_M are displayed as a function of the axial position x/H. D_R is greater than D_L and D_M by a factor of more than 40. Thus, the Leonard stresses and the cross-stresses may be neglected in our calculations. This result corroborates the

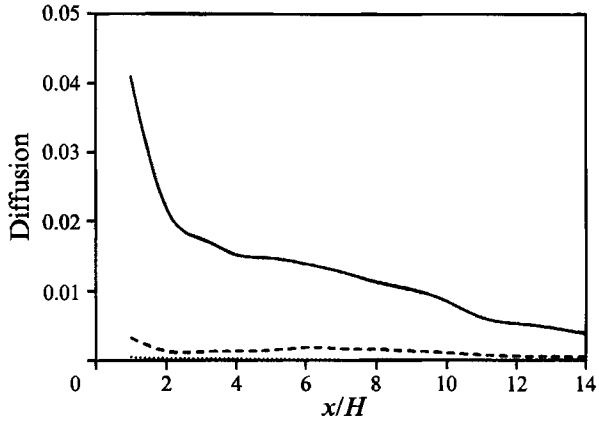

FIGURE 2. Distribution of diffusion maxima (in each vertical section): subgrid Reynolds diffusion, D_R (solid line); Leonard diffusion, D_L (dashed line) and molecular diffusion, D_M (dotted line).

findings of Antonopoulos-Domis (1981) who also use finite-volume discretization techniques. Finally, the transport equations, including an equation for a passive temperature, take the following form:

$$\frac{\partial \bar{u}_i}{\partial t}+\frac{\partial}{\partial x_j}(\bar{u}_i \bar{u}_j)=-\frac{1}{\rho_0}\frac{\partial \bar{p}}{\partial x_i}+\frac{\partial}{\partial x_j}[2\nu S_{ij}+\tau_{ij}], \tag{2.18}$$

$$\frac{\partial \bar{T}}{\partial t}+\frac{\partial}{\partial x_j}(\bar{u}_j \bar{T})=\frac{\partial}{\partial x_j}\left(\kappa\frac{\partial \bar{T}}{\partial x_j}+\tau_{jT}\right), \tag{2.19}$$

$$\frac{\partial \bar{u}_i}{\partial x_i}=0, \tag{2.20}$$

where $\tau_{jT}=-\overline{u_i' T'}$ is the temperature turbulent flux. It is modelled as

$$\tau_{jT}=\kappa_t(\partial \bar{T}/\partial x_j), \tag{2.21}$$

with a turbulent Prandtl number $\nu_t/\kappa_t=0.6$ (see Herring *et al.* 1982; Lesieur 1990).

2.3. *Numerical algorithm*

The filtered equations (2.18)–(2.20) are solved using the TRIO code, developed by Grand *et al.* (1988). The finite-volume version of this code is used. Pressure and velocity components are defined on different nodes of a staggered grid. The time discretization is a forward-marching procedure. The continuity equation, the pressure term in the momentum equation and the boundary conditions are evaluated at the new time step, whereas the other terms of the momentum equation are evaluated at the old time step. The CFL number

$$\max_{(x)}\left[\frac{|\bar{u}|}{\Delta x/\Delta t}+\frac{|\bar{v}|}{\Delta y/\Delta t}+\frac{|\bar{w}|}{\Delta z/\Delta t}\right]$$

is kept below 0.5 to ensure time-accurate integration.

The discrete form of (2.18) and (2.20) leads to a linear algebraic system. Taking the divergence allows the unknown velocities to be eliminated. The new equation is similar to a discrete form of a Poisson equation for the pressure. This algorithm was originally proposed by Hirt, Nichols & Romero (1975) and is known as the SOLA method. We

Run	Classification	Resolution ($x \times y \times z$)	Aspect ratio $R = W/H$	Reynolds number	Turbulence model
2DEUa	2D	320×40	1.25	6000	No model
2DEUb	2D	320×80	2.5	38000	No model
2DKEP	2D	240×20	2.5	38000	K–ϵ
3DEUa	3D	$130 \times 25 \times 40$	1.25	6000	No model
3DEUb	3D	$90 \times 16 \times 16$	2.5	38000	No model
3DFSa	3D	$130 \times 25 \times 40$	1.25	6000	Struc. function
3DFSb	3D	$90 \times 16 \times 16$	2.5	38000	Struc. function
3DFSc	3D	$200 \times 30 \times 30$	2.5	38000	Struc. function
3DSMA	3D	$90 \times 16 \times 16$	2.5	38000	Smagorinsky

TABLE 1. Classification of the numerical experiments: geometry, resolution, two- (2D) or three-dimensional (3D) and Reynolds number. The Reynolds number is defined as $Re_H = U_0 H/\nu$; H and W are shown in figure 1.

introduced two main differences with respect to the SOLA method: (*a*) the Poisson equation is solved with a direct method, (*b*) the discrete form of the convective terms is derived from a third-order approximation, the SMART scheme (Gaskell & Lau 1988). A third-order convective transport scheme is necessary in order to avoid excessive numerical diffusion.

Having defined the various parameters of the calculation, we will now validate the numerical method in the two-dimensional laminar flow regime.

2.4. *Flow configuration and boundary conditions*

As shown on figure 1, H and W are respectively the step and channel heights, the aspect ratio being defined as W/H. We define what we call the 'low-step' and 'high-step' cases: the low step has an aspect ratio of 2.5 and corresponds to the same step geometry as in the laboratory experiments by Eaton & Johnston (1980). In the high-step case, the aspect ratio is 1.25.

2.4.1. *Inflow*

To limit the number of computational grid points, the inlet channel is not simulated and the inflow conditions are imposed at the step ridge: the flow consists of a mean velocity field $U(y)$ on which is superimposed a white noise ξ of amplitude $10^{-4} \max(U(y))$. The noise intensity is slightly lower than the free-stream turbulence level upstream of the step measured in Eaton & Johnston's (1980) experiment (between 0.3 and 0.4% at $x/H = -1.5$).

For the low-step configuration, $U(y)$ corresponds to the profile given by Eaton & Johnston (1980, p. 159) in their high-Reynolds-number case. U_0 denotes the inlet velocity outside the boundary layer. In our numerical runs of this low-step case, the Reynolds number Re_H based upon U_0, H and the molecular viscosity is 38000. The corresponding momentum-thickness-based Reynolds number Re_θ of the separating boundary layer is 852. The run parameters are shown in table 1. $U(y)$ will be taken uniform ($\equiv U_0$) in the high-step case. In that case, $Re_H = 6000$.

The white noise roughly models the residual turbulence within the upstream flow. In our calculations, in fact, the backward-facing step flow is always unstable, even without the inlet perturbation. Similar behaviour was obtained in two-dimensional numerical simulations of the spatial mixing layer by Buell & Huerre (1988). Since these mixing layers are convectively unstable, it is the outflow boundary condition (see below) that forces pressure perturbations upstream. Therefore, our calculations might

be more of the forced-transition than the natural-transition type. Previous numerical studies have shown that the flow characteristics are very sensitive to small changes in the inlet conditions (e.g. Kaiktsis, Karniadakis & Orszag 1991). However, the work of Arnal & Friedrich (1993) has demonstrated the difficulty in precisely matching experimental inflow conditions such as turbulence intensities. In order to minimize the number of discretization points devoted to the inlet channel, we have therefore chosen the *synthetic* inflow boundary conditions described above: in the downstream flow near the step, these allow a realistic mean flow field to be reproduced (figure 18), when the turbulent intensity is slightly underpredicted as compared to Eaton & Johnston's (1980) data (figure 21).

The inlet boundary condition for the passive temperature is such that T_c ('cold fluid') and T_h ('hot fluid') are imposed respectively at 15% and 85% of the inlet channel, as illustrated by figure 1(*b*). For the three-dimensional experiments, this condition is taken uniform in the spanwise direction.

2.4.2. *Outflow*

At the outlet, the longitudinal velocity gradients are taken equal to zero, and a hydrostatic pressure distribution is assumed. This outflow boundary condition requires that the flow must be completely developed. In order to ensure this condition, the outlet of the channel is placed far from the region of interest ($x/H > 12$) with the aid of an expanding mesh. In most of the cases, we took $X_{out}/H \approx 30$, where X_{out} is the total length of the channel.

2.4.3. *Upper and lower boundaries*

The boundary condition at the solid walls poses serious problems: the no-slip condition is the most natural choice, but it requires a very fine mesh near the wall. For instance, Piomelli (1988) uses $\frac{1}{3}$ of the total grid points to simulate the wall region of a channel flow. In our study, since we focus on the detailed analysis of the turbulent structures present in the whole flow, including those within the shear layer behind the step, the mesh points have to be distributed more uniformly across the height of the channel. Therefore, the first mesh point cannot be set near the wall in the viscous sublayer, where the exact form of the no-slip condition can be written. Instead, the first mesh point is located in the turbulent part of the boundary layer. The total shear stress is assumed constant across the interval between the wall and the first mesh point and equal to the wall shear stress. The evaluation of the wall shear stress is based upon the assumption of a logarithmic velocity profile in the inertial part of the turbulent boundary layer. We use the conventional logarithmic law:

$$U = u^* \left[\frac{1}{\kappa} \ln \left(\frac{y u^*}{\nu} \right) + 5 \right], \tag{2.22}$$

where κ is the von Kármán constant ($\kappa = 0.4$). As shown by Ciofalo & Collins (1989), this assumption is partially invalidated in the recirculation region and just downstream of the reattachment zone: the velocity profile follows a logarithmic law with the same slope but a different magnitude than in the turbulent boundary layer with no pressure gradient. For simplicity, the logarithmic velocity profile along a flat plate is used hereafter in the evaluation of the wall shear stress. We believe that this does not introduce a significant error in the development of the turbulent flow in the mixing layer and in the recirculation region away from the immediate vicinity of the wall: indeed, this flow is largely controlled by inflexional instabilities behind the step. This boundary condition can be considered as an intermediate between no-slip and free-slip

conditions. Numerical constraints prevent the exact prescription of the former, while the latter may lead to artificial pressure and vorticity sheets near the wall. The following results should be validated with respect to new experiments, and higher-resolution calculations when computers will permit. Note that the same doubts as for the logarithmic condition may be brought to the role of the outflow boundary condition, which forces the flow as already stressed. Note finally that experiments are not free of unwanted forcing, due for instance to a feedback between outgoing vortices and upstream perturbations.

2.4.4. *Lateral boundaries*

Recent large-eddy simulation computations by Arnal & Friedrich (1993) have demonstrated an influence of the channel width on the flow statistics, when periodic boundary conditions are used in the span. However, they have also shown that incomplete grid resolution in the simulations can lead to large discrepancies between experimental and numerical studies. The available computer resources oblige us to find a compromise between large spanwise extent and fine grid resolution: here, we have chosen to limit the channel width. In the low-step case, we take the spanwise extent of the computational domain L_z equal to the channel height W (see figure 1*a*): this corresponds to about $\frac{1}{3}$ of the corresponding length of Eaton & Johnston's (1980) experiment. Therefore, in order to reduce the perturbation caused by this limited extent, a free-slip and impermeability condition is imposed such that $\partial u/\partial z = 0$, $\partial v/\partial z = 0$ and $w = 0$ on the lateral planes. The good agreement for the re-attachment length between the experimental data and the numerical predictions with the fine mesh (see §4.2) seems to justify this choice. For the high-step case we take $L_z = 2W$, and a periodic boundary condition is used. Here, we focus on the topology of the flow and in particular on its spanwise pattern. The results presented in §3.2 show that the wavelength of this pattern is substantially smaller than the spanwise size of the computational domain, indicating that the flow structure is not affected by the periodic domain. Our approach is somewhat similar to the one initiated by Jimenez & Moin (1991) in their *minimal channel* study: it consists of studying in detail the morphology of the flow structures that contribute the most to the turbulent flow dynamics.

2.5. *Validation of the numerical method*

In order to validate the method, it is of interest to evaluate, in the two-dimensional laminar flow regime, the Reynolds-number dependence of the re-attachment length, for which several experimental and numerical results exist. In figure 3, we present the numerical results of two-dimensional calculations performed with the TRIO code: we have chosen a flow geometry with an expansion ratio $W/H = 1.94$ (see figure 1) corresponding to the laboratory experiment of Armaly *et al.* (1983) (resolution 100×40). We find a very good agreement with the recent numerical works of Kaiktsis *et al.* (1991). The computed length compares very well with the experimental data at small Reynolds number. However, whatever the numerical approach followed, the re-circulation length is underestimated above Reynolds numbers $Re \approx 500$: this is the threshold above which the experimental flow becomes three-dimensional in the region downstream of the step.

2.6. *Description of the numerical runs*

We have carried out two- and three-dimensional calculations corresponding to the low- and high-step cases. Some were performed without any subgrid-scale model: these computations are not direct numerical simulations, in the sense that numerical

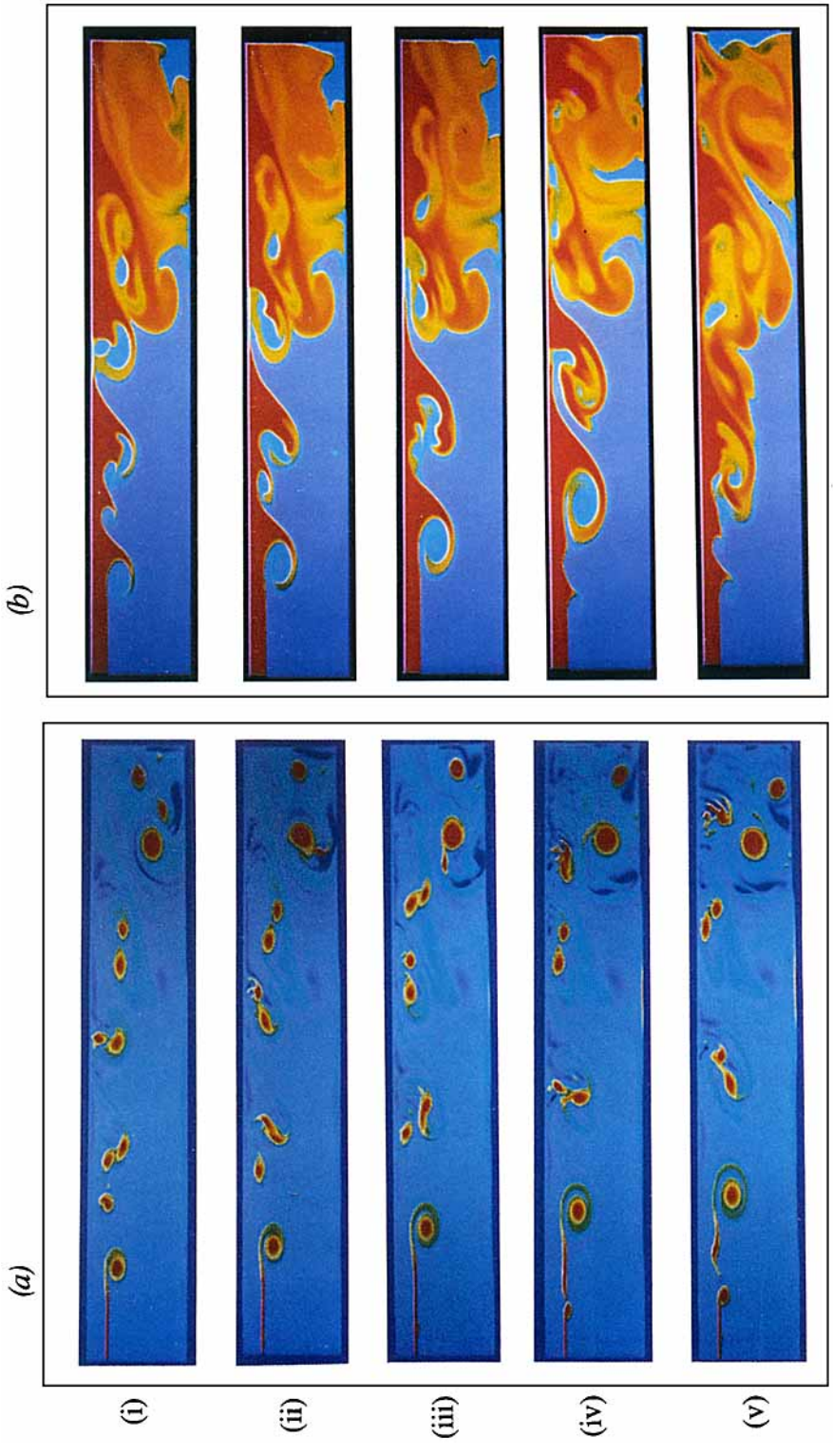

FIGURE 4. Temporal evolution of the two-dimensional flow; high-step case (run *2DEUa*). *(a)* Spanwise vorticity ω_z (red: $\omega_z > 0$ and dark blue: $\omega_z < 0$). *(b)* The same calculation as in *(a)* but for the temperature field (red: T=1 and blue: T=0). (i) t=102H/U_0; (ii) t=104H/U_0; (iii) t=106H/U_0; (iv) t=108H/U_0; (v) t=110H/U_0.

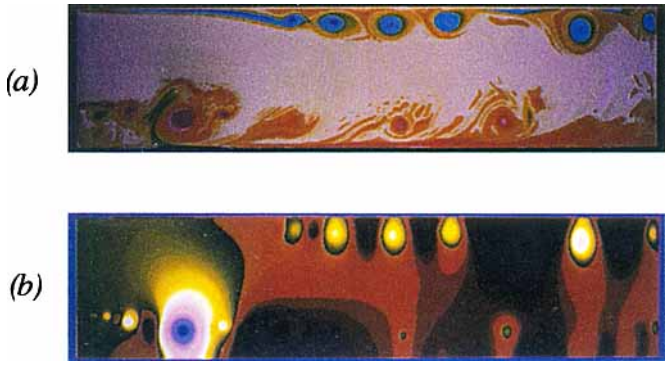

FIGURE 5. Unsteady two-dimensional flow; low-step case (run 2*DEUb*): *(a)* Spanwise vorticity field ω_z (red: $\omega_z > 0$ and blue: $\omega_z < 0$); *(b)* pressure field (blue and light colours: low-pressure centres; dark colours: high-pressure centres). $t=200H/U_0$.

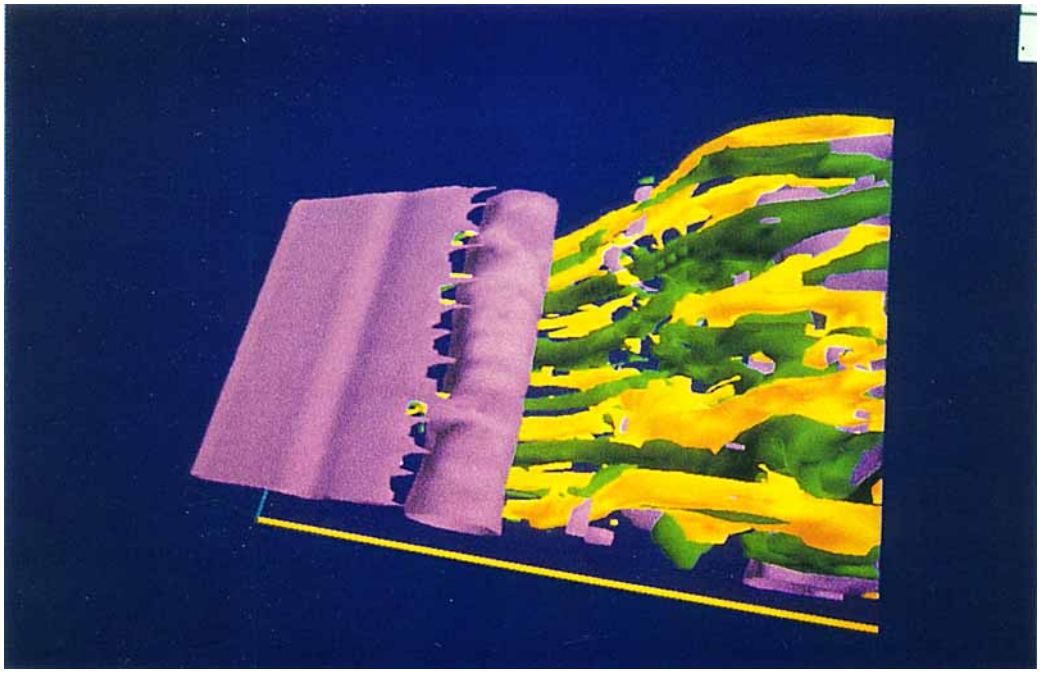

FIGURE 6. Unsteady flow downstream of the backward-facing step at $t=140H/U_0$; purple: spanwise vorticity, $\omega_z=2.0U_0/H$; yellow: streamwise vorticity $\omega_x=+0.8U_0/H$; green: streamwise vorticity $\omega_x=-0.8U_0/H$; Euler simulation (run 3*DEUa*).

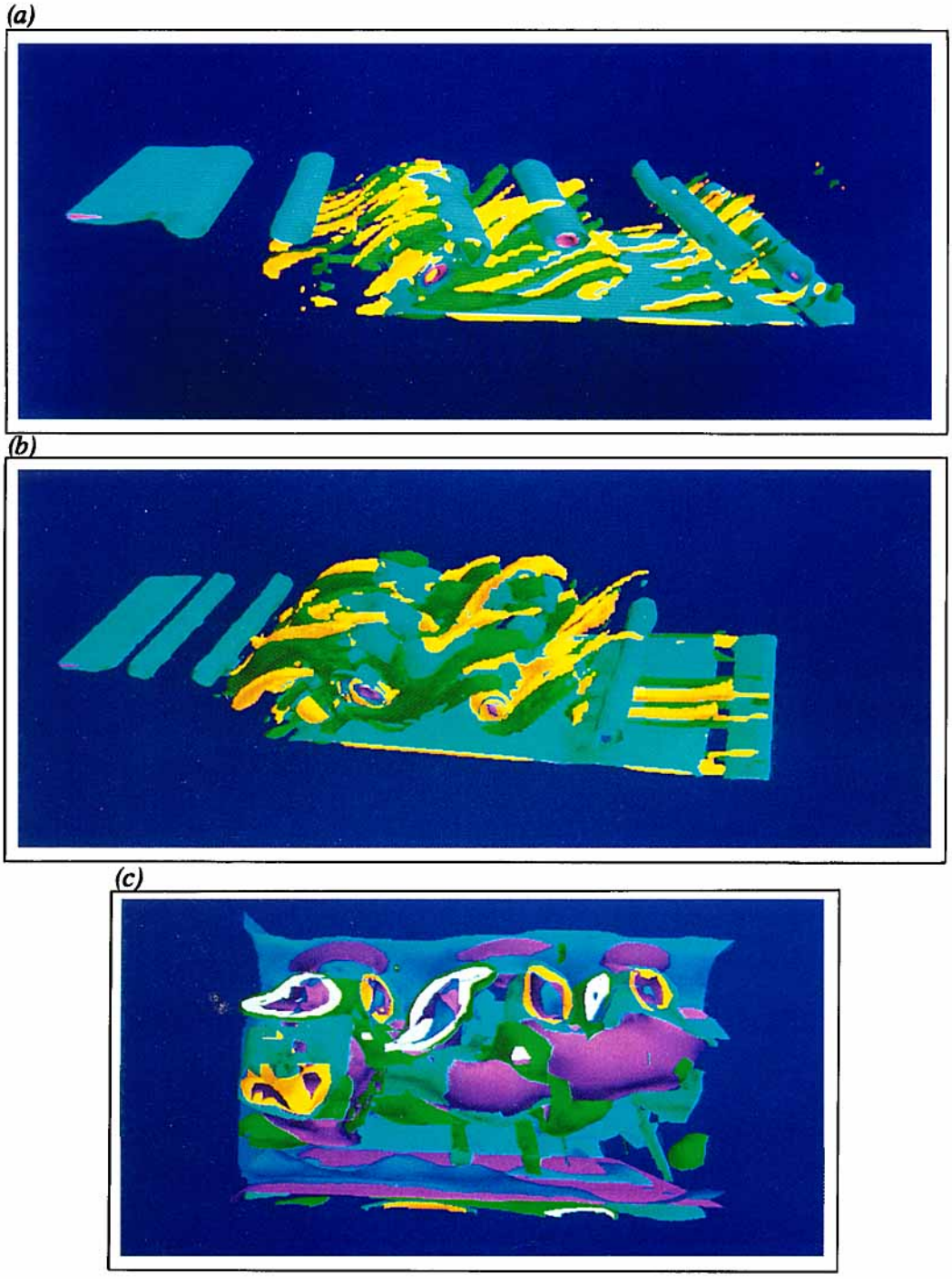

FIGURE 7. Unsteady three-dimensional flow; high-step case (run 3*DFSa*): *(a)* t=130H/U_0; light blue: vorticity modulus $||\underline{\omega}||$=1.8U_0/H; yellow: streamwise vorticity ω_x=+0.8U_0/H; green: streamwise vorticity ω_x= −0.8U_0/H; *(b)* t=138H/U_0; *(c)* cross-section in the *(y,z)*-plane, between the second and the third spanwise vortices in *(b)*; view of the streamwise counter-rotating vortices.

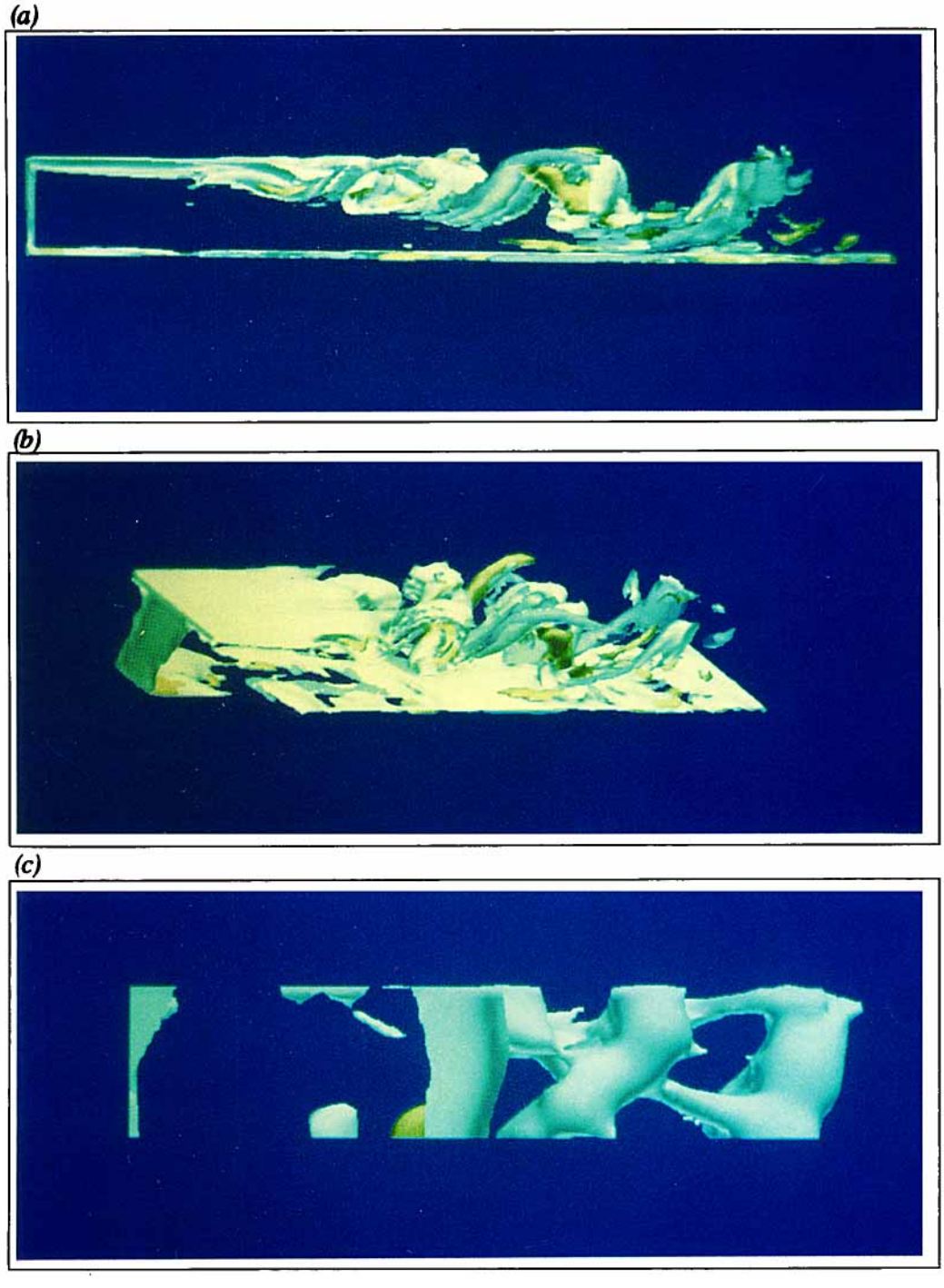

FIGURE 10. Unsteady three-dimensional flow; low-step case (run 3*DFSc*,); $t=90H/U_0$; *(a), (b)* light blue: vorticity modulus $\|\underline{\omega}\|=3.5U_0/H$; dark blue: streamwise vorticity $\omega_x=+2.5U_0/H$; green: $\omega_x=-2.5U_0/H$; *(c)* top view of the isobar $p'=-0.3\rho_0 U_0^2$.

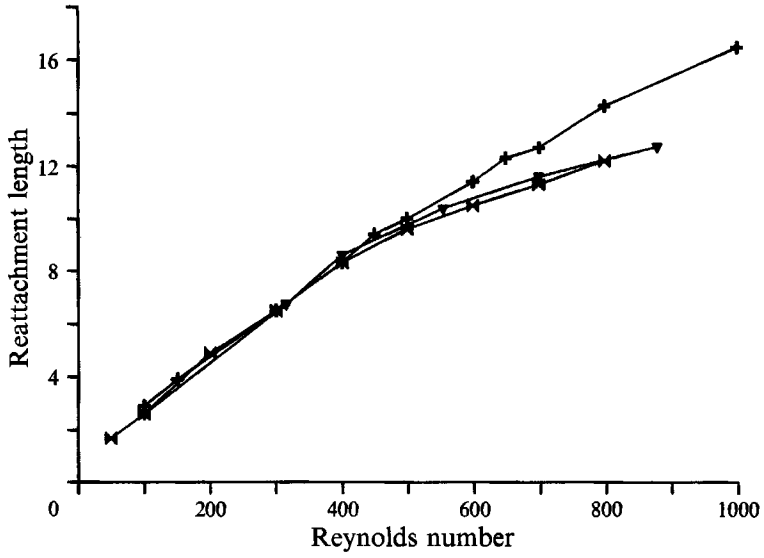

FIGURE 3. Re-attachment length normalized by the step height versus Reynolds number for Armaly *et al.*'s experiment (+) and two-dimensional (laminar) simulations of Kaiktsis *et al.* (⋈) and using TRIO (▼).

viscosity damps to some extent the cascade of energy fluctuations towards the smallest resolved scales. It is more of the type of an 'Euler computation', following a terminology used in computational aerodynamics.

The run characteristics are summarized in table 1. In the low-step case, we first carried out a two-dimensional Euler computation (run 2DEUb). This was then completed by a two-dimensional K–ϵ modelling calculation (run 2DKEP). In three dimensions, we first ran a low-resolution Euler computation (run 3DEUb). The other three-dimensional calculations corresponding to this geometry were large-eddy simulations: at low resolution, two subgrid-scale models were considered – the structure-function model (run 3DFSb) and Smagorinsky's model (run 3DSMA). Finally, the study was completed with a high-resolution simulation with the structure-function model (run 3DFSc).

Similarly, we first performed an Euler computation in the high-step case, both in two (run 2DEUa) and three dimensions (high resolution, run 3DEUa). For this case, we performed only one large-eddy simulation with the structure-function model (high resolution, run 3DFSa).

3. Flow structures

3.1. *Two-dimensional simulations*

We start with run 2DEUa (high step, no model). Figure 4(*a*) (plate 1) shows a temporal evolution of the flow, visualized with the aid of isovorticity contours. The flow dynamics in this case is very similar to the free mixing layer. Kelvin–Helmholtz eddies are clearly shed behind the step, and pair, as in Winant & Browand's (1974) experiment.

The diffusion of a passive temperature is also simulated, at a molecular Prandtl number of 1. It is used as a numerical dye. The upstream profile (a step) is described above and shown on figure 1(*b*). Figure 4(*b*) (plate 1) illustrates the mixing of the

temperature field corresponding to figure 4(*a*). Red and blue colours represent respectively T_h and T_c. In fact, our visualization compares very well with the back-step experiment of Gharib & Derango (1989), performed on a two-dimensional liquid film.

In the low-step case (run 2DEUb), vorticity and pressure plots shown on figure 5 (plate 2) indicate again the presence of a mixing layer behind the step. The re-attachment length x_R is found to be equal to $6.8H$ (temporal mean), against $7.8H$ as measured by Eaton & Johnston (1980). In the computation, the eddies which impinge on the lower wall, and are transported downstream, are shed with a frequency f corresponding to a Strouhal number $S = fH/U_0 \approx 0.09$. This is in good agreement with Eaton & Johnston's (1980) experiment, $S \approx 0.07$.

An interesting phenomenon in this low-step case is the separation of the boundary layer from the upper wall: it generates a second street of coherent vortices which are transported toward the outlet of the channel with a Strouhal number $S \approx 0.07$. Armaly *et al.* (1983) have also shown, in their laboratory experiment, that separation could occur on the opposite wall of a sudden expansion.

The pressure charts of figure 5, taken at $t = 200H/U_0$, show depressions (blue, white and yellow) corresponding to the coherent vortices, and high-pressure regions (dark) in between. We also see that the bottom separated shear layer curves sharply downward in the re-attachment zone and impinges on the wall. The shear layer is subjected to the effects of stabilizing curvature, adverse pressure gradient (as shown on figure 5*b*) and strong interaction with the wall in this region. These mechanisms cause a rapid decay of the turbulent kinetic energy and Reynolds stresses in the re-attachment zone, as will be shown later in the section on turbulence statistics.

A more general two-dimensional numerical simulation of the backward-facing step, including the effect of a stable stratification on the mixing layer, is presented in Silveira Neto, Grand & Lesieur (1991). In the stratified experiment, it was confirmed that the stable stratification inhibits the growth of vortices at a local Richardson number of the order of 0.25. At a high Richardson number, internal gravity waves form.

3.2. *Three-dimensional simulations*

In the mixing-layer experiments of Breidenthal (1981), Bernal & Roshko (1986) and Lasheras & Choi (1988), it was shown that secondary hairpin vortices were stretched between the primary Kelvin–Helmholtz rolls. As far as the statistical measurements are concerned (spreading rate, kinetic energy, Reynolds stresses, etc.), the laboratory experiments behind a step of infinite height carried out by Wygnanski & Fiedler (1970) have shown a very good agreement with experiments downstream of a splitter plate. Here we will study, both from a structural and a statistical point of view, the cases of both a high step and a low step, in order to examine the influence of the step height and the lateral walls upon the three-dimensional mixing-layer dynamics. The present section focuses on the flow topology; statistics are presented in the next section.

3.2.1. *High step*

We first carried out an Euler calculation in the high-step case (run 3DEUa). The corresponding vorticity field is shown on figure 6 (plate 2). It shows quasi-two-dimensional rolls shed behind the step, and longitudinal vortices of alternate sign stretched by the flow. These vortices seem to merge downstream, where the primary vortices pair.

The three-dimensional large-eddy simulations using the structure-function model ((2.8), (2.13) and (2.15)) are now looked at. The numerical experiments performed are described in table 1 (runs 3DFSa and 3DFSc).

(*a*)

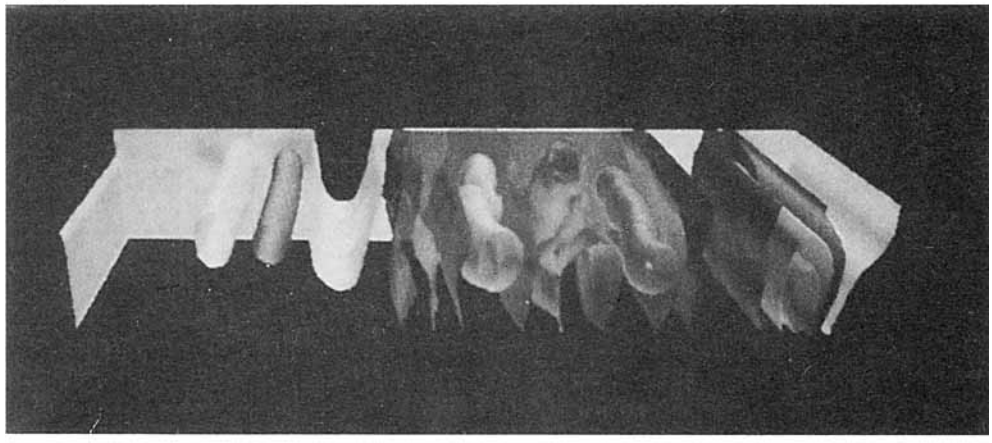

(*b*)

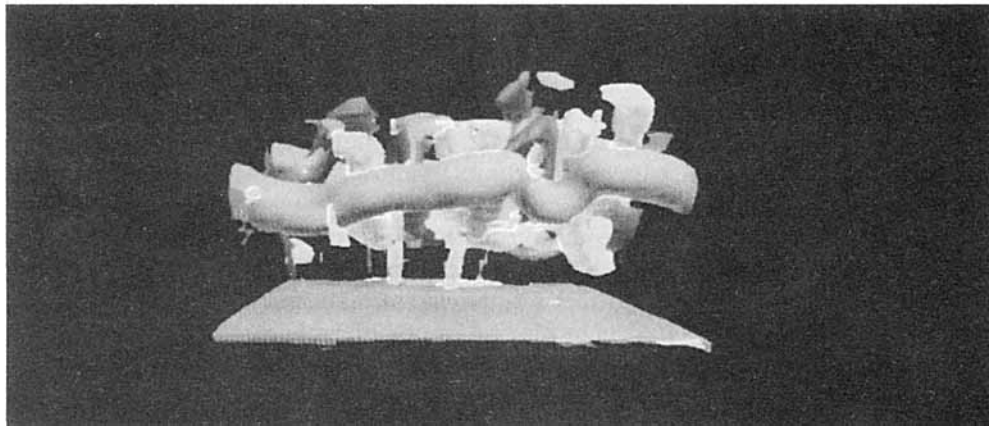

FIGURE 8. Same simulation as in figure 7(*b*): (*a*) pressure fluctuations: $p' = -0.1\rho_0 U_0^2$ and $-0.05\rho_0 U_0^2$ (light grey), $p' = 0.05\rho_0 U_0^2$ and $0.1\rho_0 U_0^2$ (dark grey and white); (*b*) vorticity field: cross-section in a (y, z)-plane between the fourth and the fifth transverse vortices in figure 7(*b*), showing a quasi-two-dimensional primary vortex (light grey: spanwise vorticity; dark and white: longitudinal vorticity).

Figures 7(*a*) and 7(*b*) (plate 3) show the vorticity field related to the higher-step experiment (3DFSa) at $t = 130H/U_0$ and $138H/U_0$ respectively. The perspective views show vorticity modulus $\|\omega\| = 1.8U_0/H$ (blue) and streamwise vorticity $\omega_x = \pm 0.8U_0/H$ (yellow and green respectively). Several primary quasi-two-dimensional spanwise vortices (blue) are convected downstream. The quasi-two-dimensionality of these vortices is obvious. Figure 8(*a*) illustrates the pressure fluctuation $p' = -0.1\rho_0 U_0^2$ (low-pressure centres) while figure 8(*b*) displays the vorticity field through a cross-section in the (y, z)-plane between the fourth and fifth spanwise vortices of figure 7(*b*). The spanwise vorticity is shown in light grey while dark and white correspond to isosurfaces of streamwise vorticity of a different sign.

Figure 7(*a*) shows a quasi-two-dimensional pairing (localized downstream of the second spanwise vortex), which is terminated at the time corresponding to figure 7(*b*). Streamwise vortices are stretched between the primary spanwise vortices (figures 7*a* and 7*b*) and are intensified as time goes on. During the pairing their spanwise period

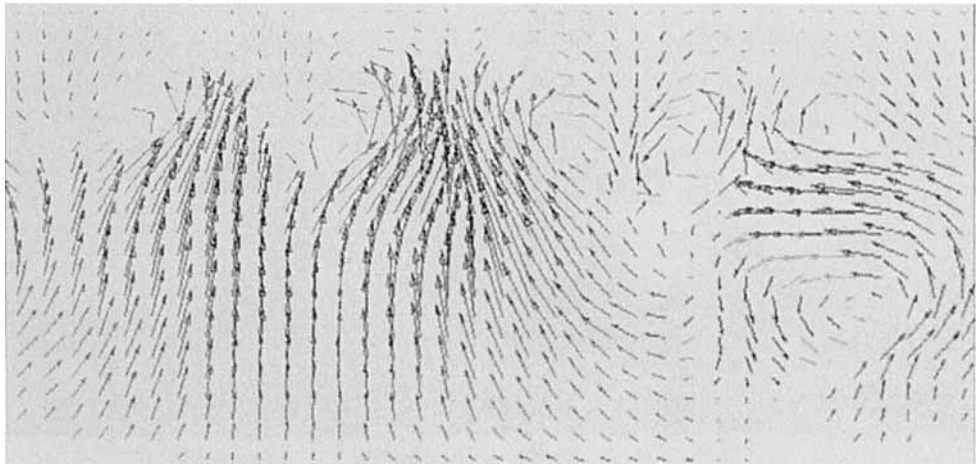

FIGURE 9. Same simulation as in figure 7(*b*): cross-section in a (y, z)-plane; projection of the large-scale velocity field $(\bar{v}, \bar{w})$, showing mushroom-shaped structures.

doubles as in Huang & Ho's (1990) experiment. Figure 7(*c*) (plate 3) shows a vertical cross-section in the (y, z)-plane of the longitudinal vortices through the braid upstream of the pairing vortices (same field as figure 7*b*). This figure clearly shows the hairpin counter-rotating vortices (streamwise vorticity; yellow: $\omega_x = +0.8U_0/H$ and white: $\omega_x = -0.8U_0/H$). In this case $\omega_x \approx 40\,\%\,\omega_z$. Figure 9 displays the velocity field in the same vertical cross-section presented above. The mushroom-shaped structure of figure 7(*c*) is reminiscent of the mixing-layer laboratory experiments (Bernal & Roshko 1986 and Lasheras & Choi 1988) and direct numerical simulations (Metcalfe *et al.* 1987).

The pairing and the hairpin vortices play an important role in the transition process toward three-dimensionality. Indeed, the hairpin vortices become part of the core of the spanwise vortex resulting from the pairing of two Kelvin–Helmholtz rolls. As observed by Bernal & Roshko (1986), these secondary instabilities (hairpin vortices) generate the three-dimensionality, while the pairing redistributes it. This is at the origin of the Kolmogorov energy cascade toward three-dimensional small scales, which we have measured and which will be presented below.

The streamwise hairpin vortices exhibited above are certainly due to the straining between the large spanwise rollers of quasi-two-dimensional vortex filaments initially located in the stagnation region. However, numerical simulations of a temporal mixing layer forced initially by a small-three-dimensional white-noise forcing have displayed a staggered mode of the 'helical-pairing type' (Comte, Lesieur & Lamballais 1992). The latter was predicted theoretically by Pierrehumbert & Widnall (1982) on the basis of a secondary instability analysis of the Stuart vortices. What we observe here for the high step seems to come from the fact (already stressed above) that our calculations might be forced artificially by the outflow boundary condition.

The local vorticity thickness δ_w of the mixing layers is defined as follows:

$$\delta_w = \frac{\langle \bar{u} \rangle_{+\infty} - \langle \bar{u} \rangle_{-\infty}}{(\partial \langle \bar{u} \rangle / \partial y)_{max}}, \tag{3.1}$$

where $\langle \bar{u} \rangle_{+\infty}$ and $\langle \bar{u} \rangle_{-\infty}$ are the extrema of the time-averaged streamwise velocity on the upper and lower sides of the mixing layer. The ratio $\lambda = s/\delta_w$, where s is the spanwise wavelength of the streamwise vortices (figure 7*c*), is in good agreement with

Bernal & Roshko's (1986) observations. We find $\lambda = 0.7$, against $\lambda = 0.8$ in the experiment. As stressed by Bernal & Roshko (1986), this value is close to the value of $\frac{2}{3}$ found for the most-amplified mode of the translative instability (global in-phase spanwise oscillation of the billows) by Pierrehumbert & Widnall (1982). It suggests that the translative instability of the Kelvin–Helmholtz billows selects the spanwise period of the hairpin vortices strained longitudinally. Notice that, in the simulation without the subgrid model, the spanwise spacing between the longitudinal vortices is much smaller (figure 6) than in the large-eddy simulation (figure 7*b*) and Bernal & Roshko's (1986) experiment. This is an argument in favour of the structure-function model.

3.2.2. *Low step*

The results of the high-resolution low-step case (run 3DFSc) are now presented. The visualization of the instantaneous flow field at $t = 90H/U_0$ is shown on figure 10(*a*, *b*) (plate 4). It displays the vorticity modulus $\|\boldsymbol{\omega}\| = 3.5U_0/H$ (light blue); the streamwise vorticity $\omega_x = +2.5U_0/H$ (dark blue) and $\omega_x = -2.5U_0/H$ (green). A plane sheet of vorticity appears just downstream of the step (left-hand side of the figure) and breaks down into intense longitudinal vortices ($\omega_x \approx 60\,\%\,\omega_z$). These streamwise counter-rotating vortices are similar to those visualized in the laboratory experiments of Kiya (1989) and Bandyopadhyay (1991). Intense longitudinal vortices were also noticed in the recent large-eddy simulations by Friedrich & Arnal (1990) with a step geometry close to the present one, $W/H = 2$. This illustrates the flow complexity in the re-attachment region, and explains the instantaneous fluctuations of the re-attachment length. These streamwise structures were also observed by Müller & Gyr (1986) and can explain the rapid entrainment of fluid upward in the downstream region of dunes.

A top view of the low-pressure field corresponding to figure 10(*b*) is shown in figure 10(*c*). It corresponds to $p' = -0.3\rho_0 U_0^2$. Three primary Kelvin–Helmholtz vortices are visible. The one closest to the step is almost cylindrical and is quasi-two-dimensional. The other two pressure tubes are strongly distorted in the spanwise direction. They are linked by two streamwise tubes, which seem to correspond to the secondary vortices shown previously in figure 10(*b*). However, it is not clear whether the vortex patterns shown on figure 10 are of the same type as for the high step (with a strong distorsion due to the lower wall), or if they are a helical-pairing type instability, as in the natural mixing-layer calculations of Comte *et al.* (1992). Notice also that the free-slip lateral boundary conditions used here might be responsible for the helical-pairing pattern. It is clear, as stressed above, that the width of the computational channel is smaller than in the experiments. New calculations in a larger channel should be undertaken in order to validate our predictions. However, the statistics of the flow shown below are encouraging, when compared with the experimental measurements.

4. Turbulence statistics

In this section we focus on the low-step case corresponding to the geometry of Eaton & Johnston's (1980) experiment.

4.1. *Two-dimensional simulations*

First, the results of the two-dimensional numerical simulation (run 2DEUb) are presented. In this run, the dimensionless Navier–Stokes equations (taking $\tau_{ij} = 0$ and $\tau_{iT} = 0$ in (2.18) and (2.19)) are integrated from the initial condition $\boldsymbol{u}(\boldsymbol{x}, 0) = \boldsymbol{0}$ and $T(\boldsymbol{x}, 0) = 0$ until a statistically steady state is reached. This equilibrium state is identified with the aid of the longitudinal velocity field, as illustrated by figures 11(*a*)

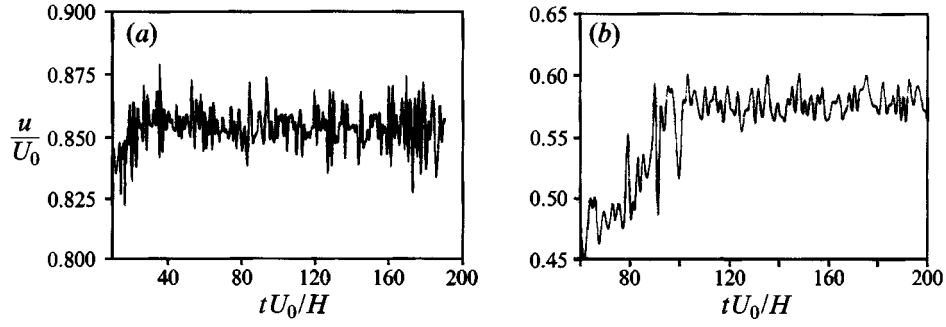

FIGURE 11. Temporal evolution of the longitudinal velocity component u; run 2DEUb. (*a*) $x/H = 3, y/H = 1$; (*b*) $x/H = 12$, $y/H = 1$.

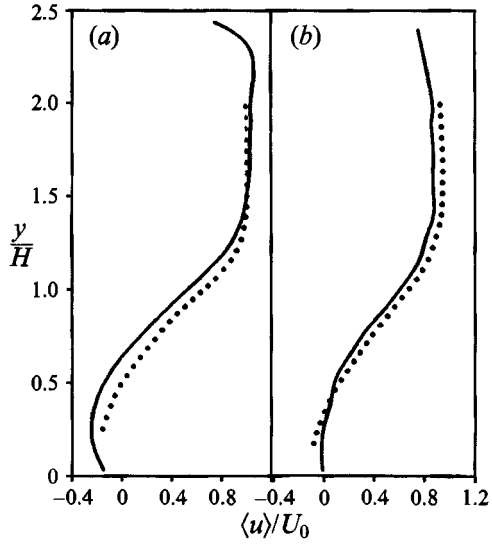

FIGURE 12. Transverse profile of the longitudinal mean velocity: straight line, run 2DEUb; dots, laboratory experiment of Eaton & Johnston (1980). (*a*) $x/H = 4$, (*b*) $x/H = 6$.

and 11(*b*). Figure 11(*a*) presents a temporal evolution of the streamwise velocity at $x/H = 3$ and $y/H = 1$ (in the mixing layer). The steady state in this case is observed for $t \sim 40H/U_0$. Figure 11(*b*) shows the streamwise velocity at $x/H = 12$ and $y/H = 1$, and in this case, the steady state is reached at $t \sim 100H/U_0$. Therefore, the evaluation of the flow statistics is started after the initial transient at $t = 160H/U_0$ and pursued over a period of $\sim 400H/U_0$. Time averages are denoted by angle brackets.

The vertical profile of the mean streamwise velocity, $\langle u \rangle$, is shown in figure 12 for two downstream positions, $x/H = 4$ and 6. Comparison with the results of Eaton & Johnston (1980) shows disagreement in the recirculation region because the reattachment length is underestimated in the calculation: $x_R/H = 6.8$ versus the experimental result, $x_R/H = 7.8$.

The turbulent kinetic energy $\langle K \rangle = \frac{1}{2}\langle u_i' u_i' \rangle$ is calculated using

$$\langle K \rangle = \tfrac{3}{4}(\langle u'^2 \rangle + \langle v'^2 \rangle), \tag{4.1}$$

where u_i' is the velocity temporal fluctuation from the mean $\langle u_i \rangle$. This equation results from the approximation for the unknown spanwise turbulent kinetic energy for a two-

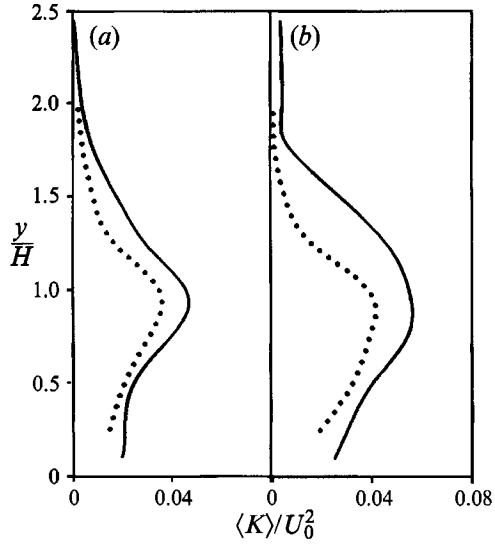

FIGURE 13. Transverse profile of the turbulent kinetic energy, same simulation as in figure 12. (*a*) $x/H = 4$, (*b*) $x/H = 6$.

dimensional simulation, i.e. $\langle w'^2 \rangle \approx \frac{1}{2}(\langle u'^2 \rangle + \langle v'^2 \rangle)$. Figure 13 shows the turbulent kinetic energy for the same downstream positions as in figure 12. The agreement with the experiment is qualitatively good, but the computed kinetic energy is significantly higher than the actual one. This is due to an excess of energy (in the two-dimensional calculation) in the v' component, since no transfer to the spanwise component is possible. Similar behaviour is observed in the two-dimensional temporal mixing layer by Lesieur *et al.* (1988).

4.2. *Three-dimensional simulations*

We first present the results for the low-resolution case. Two subgrid models are compared: the structure-function model (run 3DFSb) and Smagorinsky's (1963) model (run 3DSMA). A calculation without any model (Euler simulation) is also given for comparison (run 3DEUb).

Smagorinsky's subgrid eddy viscosity is given by

$$\nu_t(x, t) = (C_S \Delta)^2 (2 S_{ij} S_{ij})^{\frac{1}{2}}, \tag{4.2}$$

where the constant C_S, determined by Lilly (1967), is 0.2 for homogeneous isotropic turbulence. Δ, the mesh size, was previously defined.

The frequency spectrum $E_{uu}(S)$ ($S = fH/U_0$ is the Strouhal number, and f the time frequency) related to the streamwise velocity at $x/H = 12, y/H = 1$ and in the symmetry plane of the channel is first presented in figure 14. This location is chosen far downstream of the re-attachment region, where the turbulence has had enough time to develop. The arrow corresponds to a Strouhal number of 0.08, corresponding to large coherent vortices, determined with the aid of higher-resolution calculations presented below. This value is close to the experimental value of 0.07 measured by Eaton & Johnston (1980).

The two large-eddy simulations exhibit a rather small $S^{-\frac{5}{3}}$ range for frequencies higher than the frequency of the large coherent vortices, which might indicate a Kolmogorov cascade towards smaller scales. On the other hand, the Euler simulation

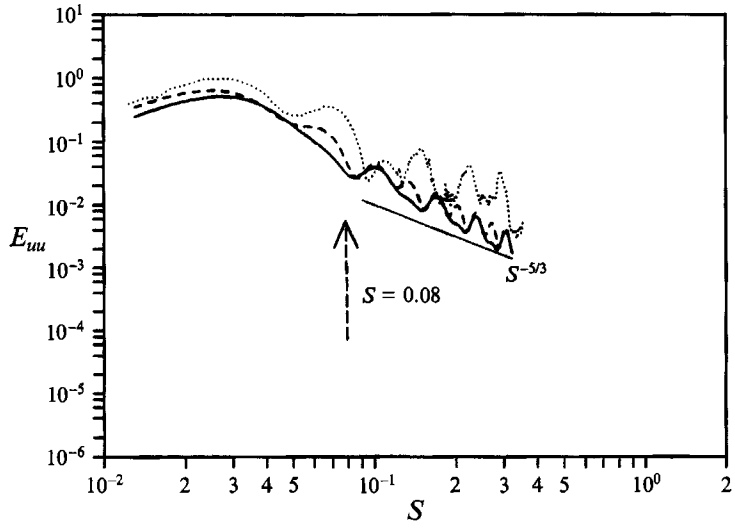

FIGURE 14. Frequency spectra of the longitudinal velocity fluctuations (the frequency f is normalized by the Strouhal number $S = fH/U_0$); $x/H = 12$, $y/H = 1$, in the symmetry plane of the channel: large-eddy simulations (structure-function (——) and Smagorinsky subgrid model (– – –)) and Euler simulation (.....) (runs 3DFSb, 3DSMA and 3DEUb). The arrow indicates the Strouhal number determined through run 3DFSc (high-resolution large-eddy simulation).

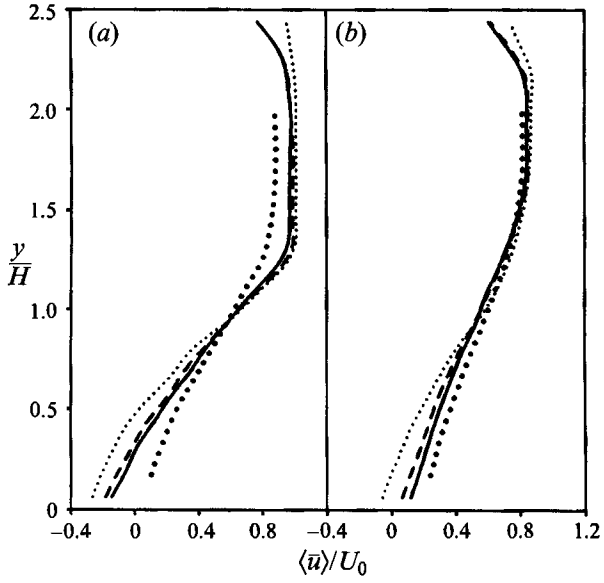

FIGURE 15. Transverse profile of the longitudinal mean velocity ($\bar{u}$) for two position x/H: (*a*) $x/H = 8$, (*b*) $x/H = 12$. Small dots, Euler simulation; dashed line, large-eddy simulation (Smagorinsky's model); solid line, large-eddy simulation (structure-function model); large dots, laboratory experiment of Eaton & Johnston (1980); same runs as in figure 14.

presents an accumulation of energy in the same frequency range. This result shows that the subgrid viscosity correctly models the kinetic energy flux through the cutoff frequency, as previously noted.

Figure 15 shows the transverse profiles of the mean streamwise velocity. The three calculations are compared with the experimental results of Eaton & Johnston (1980).

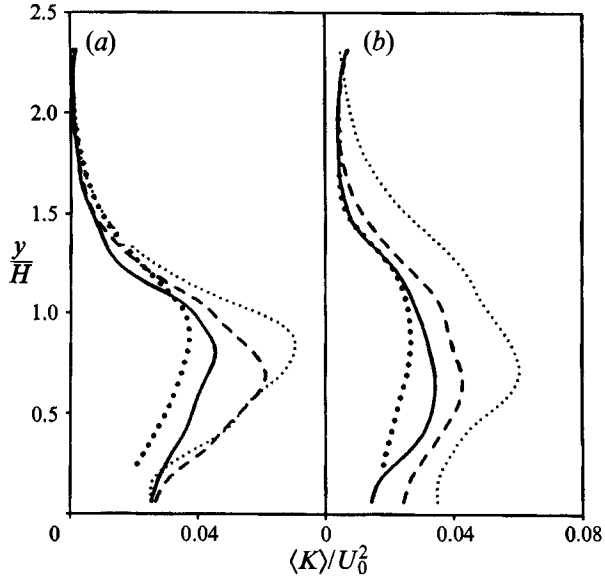

FIGURE 16. Same calculation as in figure 15: transverse profile of the turbulent kinetic energy. (*a*) $x/H = 8$, (*b*) $x/H = 12$.

The large-eddy simulation exhibits better results than the Euler simulation. However, comparison of the calculated velocity profiles with the laboratory experiment shows discrepancies in the wall region. Contrary to the two-dimensional calculation, the re-attachment length (in this low-resolution experiment) $x_R/H \sim 10$ is bigger than the experimental result. It seems that the three-dimensional effects increase this length. This poor prediction is attributed to the low resolution, which is insufficient to describe the mixing-layer dynamics that determine the velocity field and the re-attachment length.

The mean total turbulent kinetic energy is evaluated at each point by a temporal integration and consists of two parts: a contribution $\langle \overline{u_i}' \overline{u_i}' \rangle$ corresponding to the fluctuations $\overline{u_i}'$ with respect to the time average $\langle \overline{u_i} \rangle$ of the instantaneous filtered field $\overline{u_i}$ on the one hand, and a subgrid kinetic energy K_s on the other hand:

$$\langle K \rangle = \tfrac{1}{2} \langle \overline{u_i}' \overline{u_i}' \rangle + \langle K_s \rangle, \tag{4.3}$$

where K_s is calculated with the aid of (2.15).

The mean total Reynolds stresses $\langle R_{ij} \rangle$ are also composed of two parts:

$$\langle R_{ij} \rangle = \langle \overline{u_i}' \overline{u_j}' \rangle + \langle \overline{u_i' u_j'} \rangle, \tag{4.4}$$

where $\langle \overline{u_i}' \overline{u_j}' \rangle$ is calculated explicitly, and the subgrid part, $\langle \overline{u_i' u_j'} \rangle$, is calculated with the aid of the subgrid model, (2.8), (2.13) and (2.15).

Figures 16 and 17 show respectively the mean total turbulent kinetic energy and mean total Reynolds stresses. These three-dimensional simulations on a coarse grid (runs 3DEUb, 3DFSb and 3DSMA) show the influence of the subgrid model. Numerical simulation without a subgrid model is affected by the energy accumulation near the frequency cutoff. As a consequence, this simulation gives the poorest agreement with the experimental results. This indicates that some of the results given by numerical codes which rely on numerical diffusion to provide the necessary damping have to be considered with caution. The structure-function model gives better results than the Smagorinsky model, with $C_S = 0.2$.

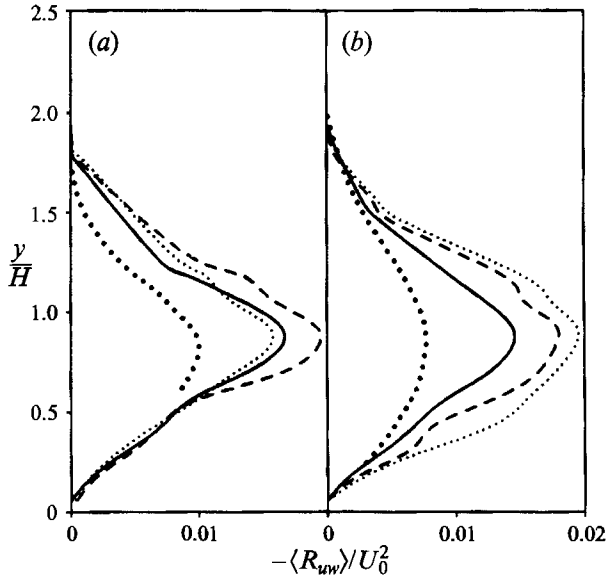

FIGURE 17. Same calculation as in figure 15: transverse profile of the Reynolds stresses. (*a*) $x/H = 8$, (*b*) $x/H = 12$.

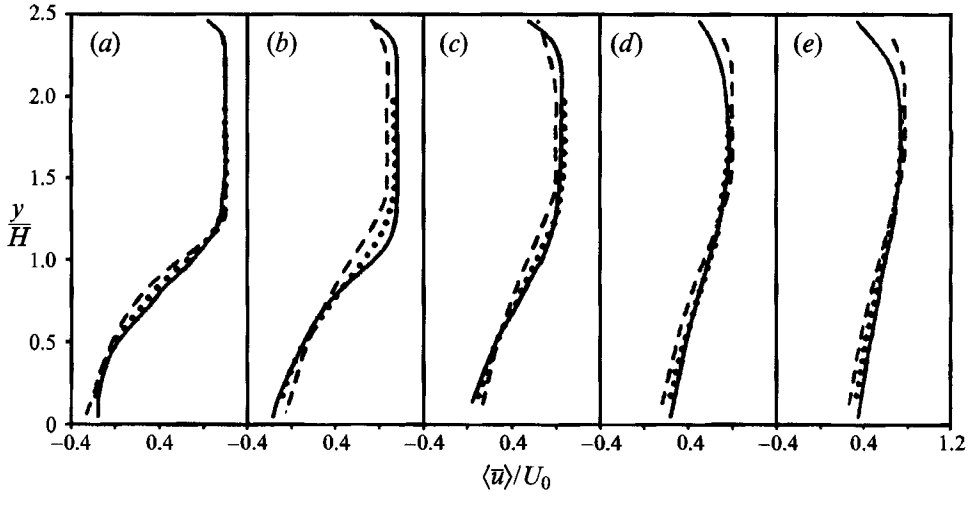

FIGURE 18. Transverse profile of the longitudinal mean velocity for five positions (x/H): (*a*) $x/H = 4$, (*b*) 6, (*c*) 8, (*d*) 10, (*e*) 12. Dashed line, K–ϵ modelling (run 2DKEP); solid line, large-eddy simulation (structure-function model, run 3DFSc); and dotted line, laboratory experiment of Eaton & Johnston (1980).

A high-resolution simulation (run 3DFSc) was attempted with the first model in order to improve the comparison with experimental results. The flow dynamics of this simulation were described in §3, and we present hereafter the flow statistics. This calculation has also been compared to a classical K–ϵ statistical model (Rodi 1982), implemented in the TRIO code (run 2DKEP). For the K–ϵ run, we have determined an *optimal* minimal resolution in the same way it is usually done in practical industrial applications: a first calculation is performed with a very loose grid; the mesh is then

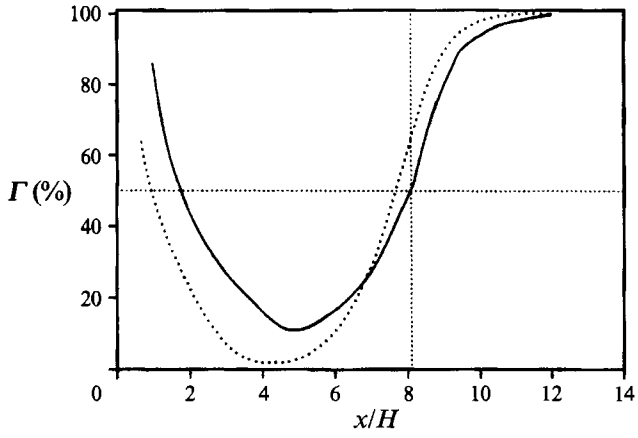

FIGURE 19. Determination of the boundary-layer re-attachment length x_R/H: solid line, large-eddy simulation (structure-function model); dotted line, laboratory experiment (typical plot) of Eaton & Johnston (1980); same run as in figure 18.

gradually refined until the results become independent of the grid resolution. The use of more computational points in the present K–ϵ computation would not modify the statistics.

The transverse profiles of the mean streamwise velocity are shown in figure 18 for five positions x/H at the symmetry plane of the channel. The agreement of the large-eddy simulation results with the experimental results is increased considerably. This is clearly demonstrated by comparison of figures 18 and 15 for two axial positions ($x/H = 8$ and 12). The results of the large-eddy simulations are globally better than those of the K–ϵ modelling.

The next result is for the boundary-layer re-attachment length x_R/H. For an unstable flow, this quantity must be determined by a statistical treatment. We define the parameter $\Gamma = \Delta t_>/\Delta t$, where Δt is the total time of integration and $\Delta t_>$ is the fraction of Δt for which the instantaneous streamwise velocity in the bottom wall is positive ($\bar{u} > 0$). The boundary-layer re-attachment length is defined as the position x_R/H, from the step, for which $\Gamma = 50\%$. Figure 19 shows $\Gamma(x/H)$ for the large-eddy simulation (structure-function model), compared with Eaton & Johnston's (1980) experiment. The results, including the K–ϵ calculation result, are:

Experiment (Eaton & Johnston, 1980)	$X_R/H = 7.8$
Large-eddy simulation (fine grid)	$X_R/H = 8.1$
K–ϵ model (grid independent result)	$X_R/H = 6.2$.

The wall pressure coefficient is defined as

$$C_p = \frac{\langle p(x,t)\rangle - p_0}{\frac{1}{2}\rho_0 U_0^2}, \tag{4.5}$$

where p_0 is the pressure at the inlet channel, related to the velocity U_0. This coefficient is presented in figures 20(*a*) (opposite wall) and 20(*b*) (step wall). The results of the large-eddy simulation are in good agreement with the experiment. In contrast, the simulation with the K–ϵ model gives a pressure recovery in a shorter distance from the step than the experiments. This leads to the underestimation of the re-circulation length. This trend was also observed by Avva, Kline & Ferziger (1988) in their K–ϵ calculations.

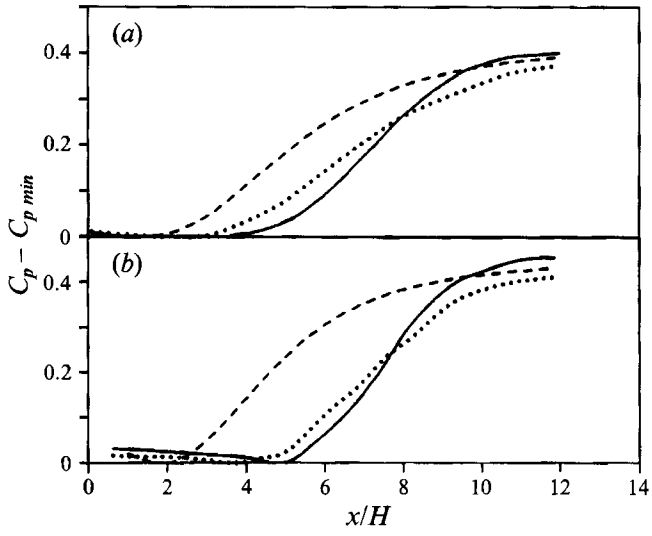

FIGURE 20. Same calculation as in figure 18: wall pressure coefficient: (*a*) opposite wall and (*b*) step wall.

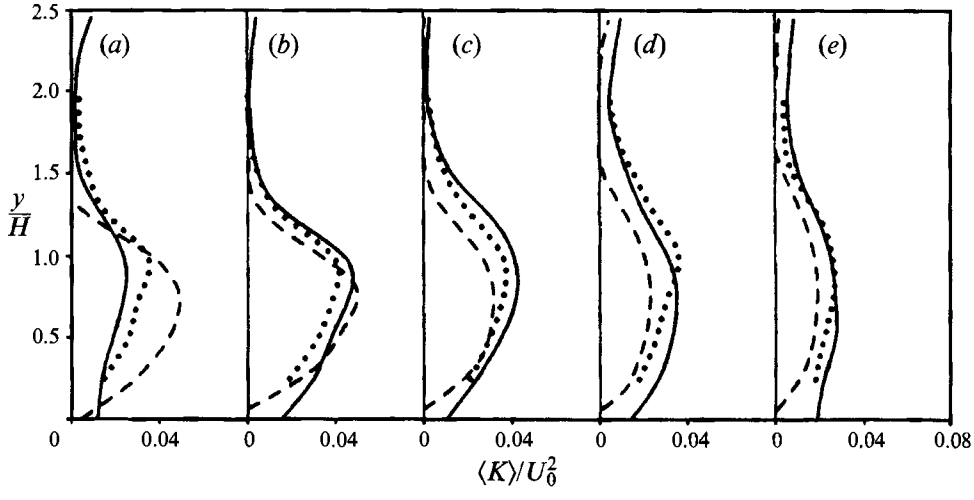

FIGURE 21. Same calculation as in figure 18: transverse profile of the turbulent kinetic energy. (*a*) $x/H = 4$, (*b*) 6, (*c*) 8, (*d*) 10, (*e*) 12.

Figures 21 and 22 show the total turbulent kinetic energy ($\langle K \rangle$) and the total Reynolds stresses ($\langle R_{uw} \rangle$). The agreement with the laboratory experiment was significantly improved with the coarse-grid simulation (figures 16 and 17). Close to the step, the position of the peak value agrees well with the experimental results. However, the differences between calculation and experiment are still large: close to separation, the characteristic scales of the instabilities are too small to be resolved explicitly. Similar trends have been noticed by other authors (see e.g. Friedrich & Arnal 1990). Furthermore, as pointed out by Friedrich & Arnal (1990), the turbulence measurements close to the step, extracted from various laboratory experiments with the same geometry, exhibit a significant scatter. Out of this region, the turbulent kinetic energy profiles computed with the aid of the structure-function model, agree well with the

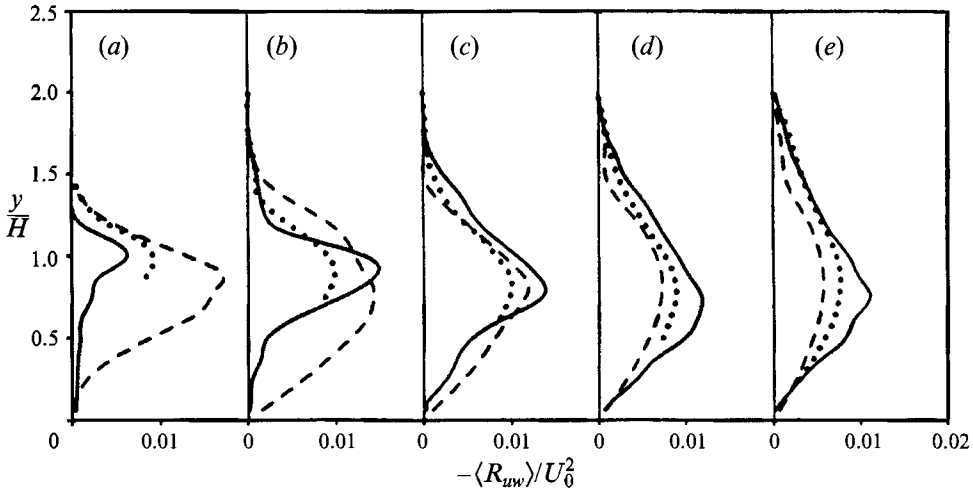

FIGURE 22. Same calculation as in figure 18: transverse profile of the Reynolds stresses. (*a*) $x/H = 4$, (*b*) 6, (*c*) 8, (*d*) 10, (*e*) 12.

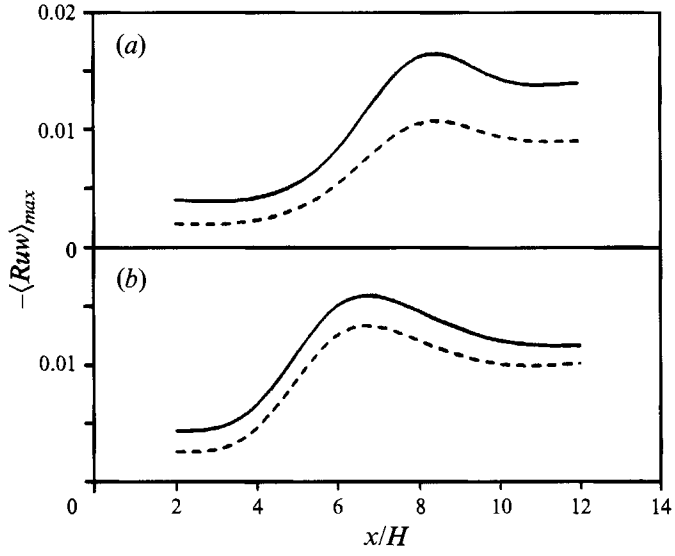

FIGURE 23. Total (solid line) and calculated (dashed line) Reynolds stresses; maxima for each transverse section: (*a*) run 3DFSb (coarse grid), (*b*) run 3DFSc (fine grid).

experiment (see figure 21) and fit the experimental uncertainty. In Eaton & Johnston's (1980) experiment, the Reynolds shear stress has been measured using a ×-array hot-wire probe: as pointed out by the authors, the hot wires undermeasure the shear stress in the region of the peak and the measurements have to be interpreted with caution. Except for the region close to the step, compared to the experimental observations the structure-function model overestimates the shear stresses near the maximum (see figure 22): this confirms Eaton & Johnston's warnings. The results of the K–ϵ model show large discrepancies in the recirculation and wall regions. However, in the free stream and downstream of the re-attachment point, the predictions are better.

The subgrid Reynolds stresses model is essential to the prediction of the total stresses. Figures 23(*a*) and 23(*b*) shows the total and explicitly calculated Reynolds

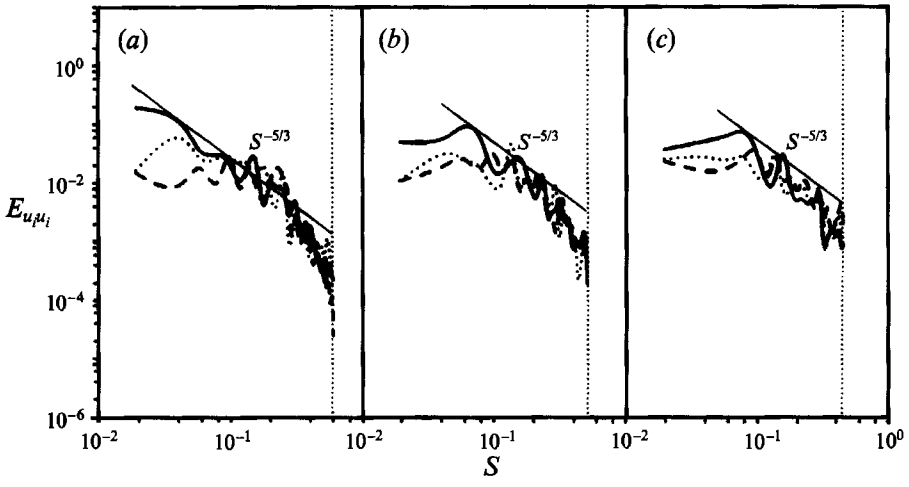

FIGURE 24. Frequency-spectra of the velocity fluctuations, large-eddy simulation (structure-function model), run 3DFSc: (*a*) $x/H = 6$, (*b*) 10, (*c*) 12. Solid line, E_{uu}; dotted line, E_{vv}; dashed line, E_{ww}.

stresses for the coarse and fine grids (runs 3DFSb and 3DFSc). These figures display the maxima of the subgrid and the total Reynolds stresses for each vertical section of the channel as a function of the streamwise position. These maxima are located slightly upstream of the re-attachment region. This trend is in agreement with the laboratory experiment of Eaton & Johnston (1980). In the neighbourhood of the step, the ratio of the subgrid stresses to the total Reynolds stresses is approximately 50% for the coarse-grid case and 40% for the fine-grid case. This ratio decreases to nearly 30% in the outlet channel for the coarse grid, and to nearly 20% in the fine-grid case. This trend was also observed by Piomelli (1988) in a large-eddy simulation of a turbulent channel flow. We also observe that in both cases the Reynolds stress decreases downstream of the re-attachment region as a consequence of the action of the stabilization effects: curvature of the mixing layer, adverse pressure gradient and interaction of the mixing layer with the wall, as observed by Bandyopadhyay (1991).

Finally, the frequency spectra for the three velocity fluctuations $\overline{u_i}'$ are plotted in figure 24. They are calculated at sections $x/H = 6$, 10 and 12, at $y/H = 1$ and in the symmetry plane of the channel. As in figure 14, they show a trend towards a $S^{-\frac{5}{3}}$ range. The energy in the smaller scales is evenly distributed among the three components, indicating a tendency towards isotropy. Indeed, this is a key point of both subgrid models (structure function and Smagorinsky's). The energy distribution in the large scales is anisotropic, and the streamwise component is the most energetic. The spectral peak of the streamwise turbulent intensity E_{uu}, for $x/H = 10$ and 12, is found at a Strouhal number $S = 0.08$. As already stressed, this value is in very good agreement with Eaton & Johnston's (1980) result, $S = 0.07$, at these streamwise positions. Several investigations of separated flows in various geometries have shown the presence of very low frequency associated with vortex shedding from the re-circulation bubble (Eaton & Johnston 1980; Arnal & Friedrich 1993). The length of the present time integration does not allow for these frequencies, good enough statistics to be obtained in order to address this issue.

5. Conclusions

A transitional complex flow downstream of a backward-facing step was simulated numerically without and with a subgrid-scale model for two- and three-dimensional situations. The numerical diffusion due to the scheme allows calculations to be performed at a very high Reynolds number. These calculations have been compared with large-eddy simulations using both the structure-function model and Smagorinsky's model.

In the high-step two-dimensional simulation (no model), we have shown that the flow is very similar to a free mixing layer, with Kelvin–Helmholtz vortices of low pressure shed behind the step and undergoing various pairings. These eddies can either bounce on the lower boundary and be advected outside the channel, or be captured by the re-circulation region. In the low-step case, the separation behind the step is responsible for the detachment of the boundary layer at the upper wall.

In the high-step three-dimensional case, we have shown that the coherent vortical structure of the flow is very close to a quasi-two-dimensionally forced mixing layer, with primary vortices shed behind the step, and secondary longitudinal hairpin vortices stretched in between. The primary vortices correspond to strong depressions. As in spatially growing mixing-layer experiments, the spanwise wavelength of the longitudinal vortices doubles at each pairing of the primary structures. The low-step large-eddy simulations using the structure-function model show dislocations in the vortices, as indicated by the low pressure field. The simulations predict a Strouhal number associated with the shedding in good agreement with experiments. Comparisons of statistical data with experiments show that the structure-function model behaves better than Smagorinsky's and K–ϵ models.

One may argue about the poor resolution close to the wall, which requires a logarithmic law to be used. This assumption is of course questionable in the re-circulation zone. However, it does not seem to inhibit the re-circulation, and certainly has a weak effect upon free-shear instabilities developing just behind the step.

For the highest resolution used here, the three-dimensional large-eddy simulations, which were performed in 1991, have consumed 60 hours of CRAY-2 CPU time. Higher-resolution simulations with mesh refinement in the wall vicinity should be undertaken on massively parallel computers. An increase in computer power should also permit testing of the effects on the flow development of various numerical parameters such as the nature of the lateral boundary conditions (free slip, periodic) and the channel width. More sophisticated outflow conditions could also be implemented (see e.g. Orlanski 1976). The inflow perturbations manipulation could allow bifurcation from one instability regime to another (from translative to helical instability for instance) and achieve an effective control of the turbulent structures. Furthermore, new laboratory experiments on the flow over a high step should be performed making use of sophisticated visualization and measurement techniques in order to scan the topology of the three-dimensional coherent vortices.

Finally, an important result of the present study is that it has demonstrated the feasibility of large-eddy simulations for industrial modelling.

The authors are indebted to the staff of LPML for developing the TRIO code, particularly to M. Villand, G. Basque and B. Frenoux. The authors thank B. Fallon for his help in the low-Reynolds-number test case. We are also grateful to Martha Grand for the revision of this manuscript. A. Silveira Neto works under a grant from CNPq (Brazil). The study was sponsored by CEA. The computations were carried out

on the CRAY-2 Machines of the Centre de Calcul Vectoriel pour la Recherche (CCVR) and Centre Grenoblois de Calcul Vectoriel (CGCV). The visualizations were performed on the IMG ALLIANT-VFX40 Machine, with the help of Y. Fouillet and E. David.

REFERENCES

ANTONOPOULOS-DOMIS, M. 1981 Large-eddy simulation of a passive scalar in isotropic turbulence. *J. Fluid Mech.* **104**, 55–79.

ARMALY, B. F., DURST, F., PEREIRA, J. C. & SCHÖNUNG, B. 1983 Experimental and theoretical investigation of backward-facing step flow. *J. Fluid Mech.* **127**, 423–496.

ARNAL, M. & FRIEDRICH, R. 1993 Large-eddy simulation of a turbulent flow with separation. In *Turbulent Shear Flows 8* (ed. F. Durst, R. Friedrich, B. E. Launder *et al.*), p. 169. Springer.

AVVA, R. K., KLINE, S. J. & FERZIGER, J. H. 1988 Computation of a turbulent flow over a backward-facing step using the zonal modeling approach. *Dept. of Mech. Engng, Stanford University, Rep.* TF-33.

BANDYOPADHYAY, P. R. 1991 Instabilities and large structures in re-attaching boundary layers. *AIAA J.* **29**, 1149–1155.

BERNAL, L. P. & ROSHKO, A. 1986 Streamwise vortex structure in plane mixing layers. *J. Fluid Mech.* **170**, 499–525.

BREIDENTHAL, R. 1981 Structure in turbulent mixing layers and wakes using a chemical reaction. *J. Fluid Mech.* **109**, 1–24.

BROWN, G. L. & ROSHKO, A. 1974 On the density effects and large structure in two-dimensional mixing layers. *J. Fluid Mech.* **64**, 775–816.

BUELL, J. C. & HUERRE, P. 1988 Inflow/outflow boundary conditions and global dynamics of spatial mixing layers. In *Proc. 1988 Summer Program – Rep. CTR-S88*, pp. 19–27. Stanford University.

CIOFALO, M. & COLLINS, M. W. 1989 k–ϵ predictions of heat transfer in turbulent recirculation flows using an improved wall-treatment. *Numer. Heat Transfer* B **15**, 21–47.

CLARK, R. A., FERZIGER, J. H. & REYNOLDS, W. C. 1979 Evaluation of subgrid models using an accurately simulated turbulent flow. *J. Fluid Mech.* **91**, 1–16.

COMTE, P., LESIEUR, M. & LAMBALLAIS, E. 1992 Large- and small-scale stirring of vorticity and passive scalar in a three-dimensional temporal mixing layer. *Phys. Fluids* A **4**, 2761–2778.

DEARDORFF, J. W. 1970 A numerical study of three-dimensional turbulent channel flow at large Reynolds numbers. *J. Fluid Mech.* **41**, 453–480.

EATON, J. K. & JOHNSTON, J. P. 1980 Turbulent flow re-attachment: an experimental study of the flow and structure behind a backward-facing step. *Stanford University, Rep.* MD-39.

FINDIKAKIS, A. & STREET, R. L. 1979 An algebraic model for subgrid turbulence in stratified flows. *J. Atmos. Sci.* **36**, 1934–1949.

FRIEDRICH, R. & ARNAL, M. 1990 Analysing turbulent backward-facing step flow with the lowpass-filtered Navier–Stokes equations. *J. Wind Engng Ind. Aerodyn.* **35**, 101–128.

GASKEL, P. H. & LAU, A. C. K. 1988 Curvature-compensated convective transport: SMART, a new boundedness-preserving transport algorithm. *Intl J. Numer. Meth. Fluids* **8**, 617–641.

GHARIB, M. & DERANGO, P. 1989 A liquid film (soap film) tunnel to study two-dimensional laminar and turbulent shear flows. *Physica* D **37**, 406–416.

GRAND, D., COULON, N., MAGNAUD, J. P. & VILLAND, M. 1988 Computation of flow with distributed resistance and heat sources. In *Proc. Third Intl Symp. on Refined Flow Modeling and Turbulence Measurements, Nipon Toshi Center Tokyo* (ed. Y. Iwasa), pp. 487–494.

HERRING, J. R., SCHERTZER, D., LESIEUR, M., NEWMAN, G. R., CHOLLET, J. P. & LARCHEVEQUE, M. 1982 A comparative assessment of spectral closures as applied to passive scalar diffusion. *J. Fluid Mech.* **124**, 411–437.

HIRT, C. W., NICHOLS, B. D. & ROMERO, N. C. 1975 SOLA – Numerical solution algorithm for transient fluid flows. *LASL Rep., Los Alamos*, LA 5852.

HUANG, L. S. & HO, C. M. 1990 Small-scale transition in a plane mixing layer. *J. Fluid Mech.* **210**, 475–500.

JIMENEZ, J. & MOIN, P. 1991 The minimal flow unit in near-wall turbulence. *J. Fluid Mech.* **225**, 213–240.

KAIKTSIS, L., KARNIADAKIS, G. E. & ORSZAG, S. A. 1991 Onset of three-dimensionality, equilibria, and early transition in flow over a backward-facing step. *J. Fluid Mech.* **231**, 501–528.

KIYA, M. 1989 Separation bubbles. In *Theoretical and Applied Mechanics* (ed. P. Germain, M. Piau & D. Caillerie), pp. 173–191. North-Holland Elsevier.

KRAICHNAN, R. H. 1976 Eddy-viscosity in two and three dimensions. *J. Atmos. Sci.* **33**, 1521–1536.

LASHERAS, J. C. & CHOI, H. 1988 Three-dimensional instability of a plane free shear layer: an experimental study of the formation and evolution of streamwise vortices. *J. Fluid Mech.* **189**, 53–86.

LEONARD, A. 1974 On the energy cascade in large-eddy simulations of turbulent fluid flows. *Adv. Geophys.* **18A**, 237–248.

LESIEUR, M. 1990 *Turbulence in Fluids*. Kluwer.

LESIEUR, M. & ROGALLO, R. 1989 Large-eddy simulation of passive scalar diffusion in isotropic turbulence. *Phys. Fluids* A **1**, 718–722.

LESIEUR, M., STAQUET, C., LE ROY, P. & COMTE, P. 1988 The mixing layer and its coherence examined from the point of view of two-dimensional turbulence. *J. Fluid Mech.* **192**, 511–534.

LILLY, D. K. 1967 The representation of small-scale turbulence in numerical experiments. *Proc. IBM Sci. Comput. Symp. Environ. Sci., IBM Data Process. Div., White Plains, NY*, pp. 195–210.

MÉTAIS, O. & LESIEUR, M. 1992 Spectral large-eddy simulation of isotropic and stably stratified turbulence. *J. Fluid Mech.* **239**, 157–194.

METCALFE, R. W., ORSZAG, S. A., BRACHET, M. E., MENON, S. & RILEY, J. J. 1987 Secondary instability of a temporally growing mixing layer. *J. Fluid Mech.* **184**, 207–243.

MOIN, P. & KIM, J. 1982 Numerical investigation of turbulent channel flow. *J. Fluid Mech.* **118**, 341–377.

MÜLLER, A. & GYR, A. 1986 On the vortex formation in the mixing layer behind dunes. *J. Hydraul. Res.* **24**, 359–375.

NORMAND, X. & LESIEUR, M. 1992 Numerical experiments on transition in the compressible boundary layer over an insulated flat plate. *Theor. Comput. Fluid Dyn.* **3**, 231–252.

ORLANSKI, I. 1976 A simple boundary condition for unbounded hyperbolic flows. *J. Comput. Phys.* **21**, 251–269.

PIERREHUMBERT, R. T. & WIDNALL, S. E. 1982 Two- and three-dimensional instabilities of a spatially periodic shear layer. *J. Fluid Mech.* **114**, 59–82.

PIOMELLI, U. 1988 Models for large-eddy simulations of turbulent channel flows including transpiration. Doctoral thesis, Stanford University.

RODI, W. 1982 Examples of turbulence models for incompressible flows. *AIAA J.* **20**, 872–879.

SILVEIRA NETO, A., GRAND, D. & LESIEUR, M. 1991 Simulation numérique bidimensionnelle d'un écoulement turbulent stratifié derrière une marche. *Intl J. Heat Mass Transfer* **34**, 1999–2011.

SMAGORINSKY, J. 1963 General circulation experiment with the primitive equations, I. The basic experiment. *Mon. Weath. Rev.* **91**, 99–164.

WERNER, H. & WENGLE, G. 1993 Large-eddy simulation of turbulent flow over and around a cube in a plate channel. In *Turbulent Shear Flows 8* (ed. F. Durst, R. Friedrich, B. E. Launder *et al.*), p. 155. Springer.

WINANT, C. D. & BROWAND, F. K. 1974 Vortex pairing: the mechanism of turbulent mixing-layer growth at moderate Reynolds number. *J. Fluid Mech.* **63**, 237–255.

WYGNANSKI, I. & FIEDLER, H. E. 1970 The two-dimensional mixing region. *J. Fluid Mech.* **41**, 327–361.